Solids Circulation Pattern and Particles Mixing in a Large Jetting Fluidized Bed

Macroscopic behavior of solids circulation in a large jetting fluidized bed was surveyed with a force probe. Particles mixing was studied by pulse injection of tracer particles, and a simple mechanistic model was developed on the basis of the solids circulation pattern observed. The model compares favorably with experimental tracer concentration profiles.

Wen-ching Yang, B. Ettehadieh and G. B. Haldipur
KRW Energy Systems, Inc.
Madison, PA 15663

Introduction

The solids circulation pattern and solids circulation rate are important hydrodynamic characteristics of an operating fluidized bed. They dictate directly the solids mixing and the heat and mass transfer between different regions of the bed.

In many applications the performance of fluidized beds is frequently controlled by the hydrodynamics phenomena occurring in the beds. Applications such as the fluidized bed combustion and gasification of fossil fuels are the cases in point. In those applications, the rates of fuel devolatilization and fines combustion are of the same order of magnitude as the mixing phenomena in a fluidized bed. The mixing and contacting of the gases and solids very often are the controlling factors in the reactor performance. This is especially true in large commercial fluidized beds where only a limited number of discrete feed points for reactants is allowed due to economic considerations. Unfortunately, solids mixing in a fluidized bed has not been studied extensively, especially in large commercial fluidized beds, because of experimental difficulties.

Earlier studies on solids mixing were reviewed by Kunii and Levenspiel (1969) and Potter (1971). A more recent review was provided by Valenzuela and Glicksman (1984). It is generally agreed that solids mixing is closely related to bubble motion in the bed. However, in most of the earlier studies the bubble flow characteristics were not simultaneously measured. To understand the solids mixing mechanisms, the experimental techniques employed need to be of fast response and to allow measurement of local tracer concentration while the fluidized bed is in operation. This study attempts to bridge some of the data gaps identified above and presents the results of solids mixing and circulation tests conducted in a large, commercial-size, jetting fluidized bed. During the experiments, the bubble characteristics were measured simultaneously with a force probe and with high-speed motion pictures. The solids samples were collected from five different sampling ports continuously during operation and thus allow almost instantaneous determination of local tracer concentration.

Correspondence concerning this paper should be addressed to Wen-ching Yang at Research and Development Center, Westinghouse Electric Corporation, Pittsburgh, PA 15235.

Experimental Apparatus and Techniques

Solids mixing and circulation rate was studied in a fluidized bed of 3 m dia. and 10 m in height by pulse injection of tracer particles with characteristics similar to those inside the bed but with sizes larger than those in the bed. By taking solids samples continuously at different bed locations and analyzing by sieving the concentration of the tracer particles in the samples, the rate of particle mixing and circulation can be calculated. Experiments were conducted in two separate bed configurations. One employed a 0.254 m jet nozzle assembly, a deep-bed configuration with a bed height of 5.5 m; a 0.406 m jet nozzle assembly was used in the second test. The bed configurations are shown in Figures 1 and 2. The central jet in the jet nozzle assembly is referred to as the solids transport tube; the middle jet as the air tube; and the outer jet as the shroud. Crushed acrylic particles -6 mesh and 1,400 μm in weight-mean average size and 1,100 kg/m^3 in density, were used as the bed material.

Altogether, four set points were carried out with air tube velocities varying from 15 to 61 m/s, employing the 0.254 m jet nozzle assembly. The operating conditions are summarized in Table 1. The bed was first operated at the preselected conditions at a steady state; then about 455 kg of the coarse crushed-acrylic particles, similar to that used as the bed material but of sizes larger than 6-mesh, were injected into the bed as fast as possible to serve as the tracer particles. Solids samples were then continuously collected from five different sampling locations, shown in Figures 3 and 4, at 30 s intervals for the first 18 min and at 60 s intervals thereafter. The samples were then sieved and analyzed for coarse tracer particle concentration. Typical tracer particle

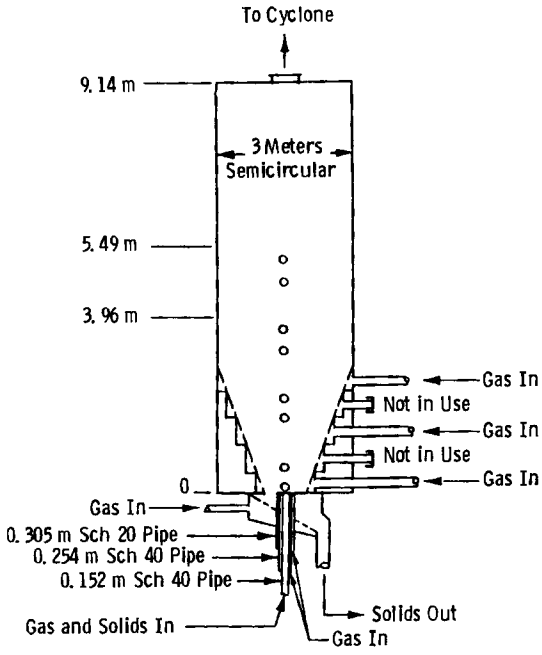

Figure 1. Bed configuration of 0.254 m jet nozzle assembly.

concentration profiles vs. time at each sampling location are presented in Figures 5 to 9 for set point 3.

Typically it took about 160 to 200 s to inject a pulse of about 455 kg coarse tracer particles into the bed pneumatically from the coaxial solid feed tube. It can be clearly seen from Figures 5 to 9 that the tracer particle concentration increases from essentially zero to a final equilibrium value, depending on the location of the sampling port. The steady state was usually reached within about 5 min. The equilibrium tracer concentrations for sampling locations *A*, *B*, and *E* are usually higher than those for

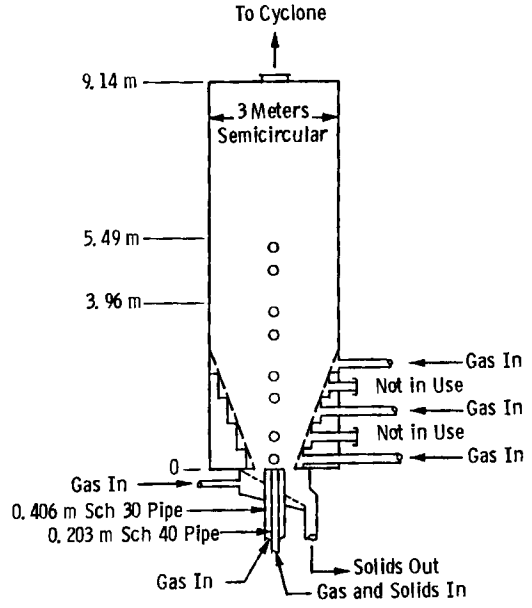

Figure 2. Bed configuration of 0.406 m jet nozzle assembly.

Table 1. Bed Operating Conditions, 0.254 m Jet Nozzle Assembly

	Set Point No.			
	1	2	3	4
Air tube flow, m^3/min*	29.7	38.7	54.6	70.9
Annular flow, m^3/min	10.2	10.2	10.5	10.5
Total grid flow, m^3/min	94.2	93.0	94.6	94.1
Solids transport flow, m^3/min	13.3	13.3	13.4	13.5
Total tracer injected, kg	459	473	473	455
Tracer injection time, s	160	200	185	157
Freeboard velocity, m/s	0.67	0.70	0.76	0.82

*Flow rates expressed at standard conditions of 20°C and 101 kPa.

locations *C* and *D*, although the difference is not substantial. This may be due to the difference in radial location of the sampling ports or it may be induced by a specific mixing pattern inside the bed. Since there was no solids sampling at different radial locations at the same bed elevation, the existence of a radial tracer concentration profile in addition to an axial profile cannot be ascertained at this time. There is considerable scatter in the data in some cases. This is to be expected because the tracer concentration to be detected is small, on the order of 4%, and absolute uniformity of mixing inside a heterogeneous fluidized bed is difficult to obtain. The current crude sampling technique can also introduce experimental scatter. Even with this difficulty, useful information on solid mixing can be obtained, as will be shown later.

Set points 1 and 3 were conducted by first passing all the bed

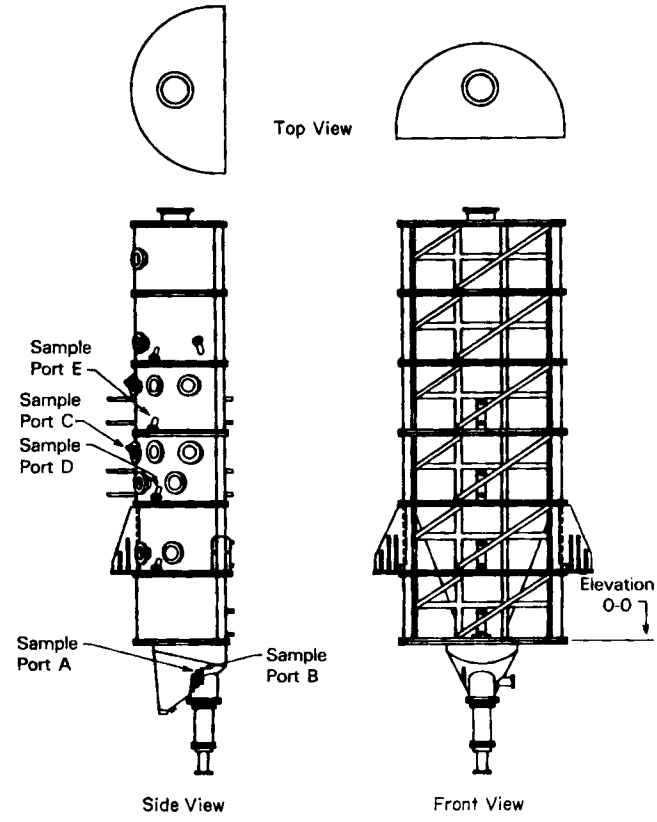

Figure 3. Deep bed configuration showing sample port locations.

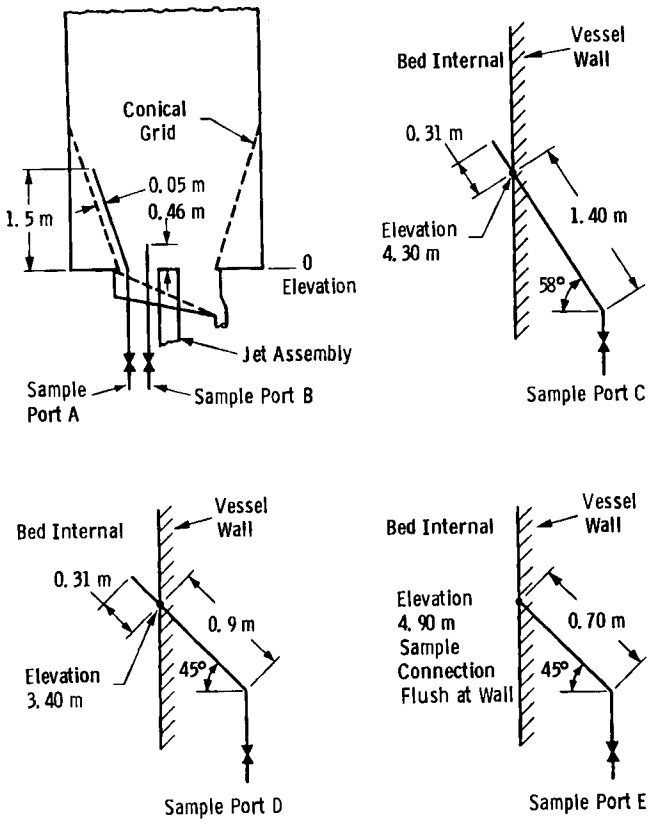

Figure 4. Sample port connections.
All sample port elevations measured from 0 elevation (= 0-0 elevation, Fig. 3).

material through a 6-mesh screen to make sure that the bed material contained no particles in the same size range as the +6 mesh tracer particles to be injected. Set points 2 and 4 were carried out immediately after set points 1 and 3 and thus the bed material already contained the tracer particles fed into the bed during set points 1 and 3. During data analysis, the data were corrected for the baseline tracer concentration at time zero using the results obtained in set points 1 and 3. Because of this

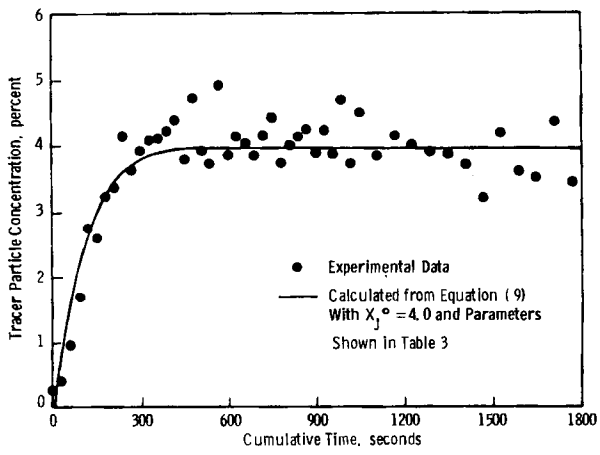

Figure 5. Experimental solids mixing data and model predictions.
0.254 m jet; set point 3; sampling port A.

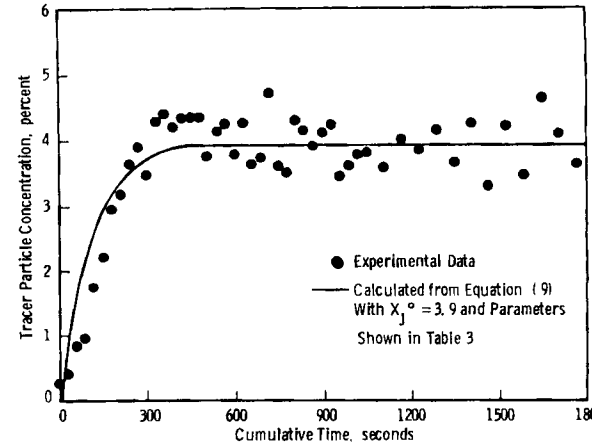

Figure 6. Experimental solids mixing data and model predictions.
0.254 m jet; set point 3; sampling port B.

additional correction, the data obtained during set points 2 and 4 tend to be less reliable.

Two set points were conducted at air tube velocities of 15 and 30 m/s using the 0.406 m jet nozzle assembly with a bed height of 5.5 m. The operating conditions are summarized in Table 2. The experiments were carried out similarly to those already described, however, only about 240 kg of coarse tracer particles were injected during each of the tests. Injection time ranged from 75 to 165 s. Bed material was passed through a 6-mesh screen and the +6 mesh material was rejected before set point 1 was conducted. Set point 2 was performed immediately following set point 1 and thus the bed material already contained the tracer particles injected during set point 1. The resulting data were corrected as discussed earlier. Typical tracer particle concentration profiles at all five sampling locations are similar to those shown in Figures 5 to 9. The data also show that the mixing is essentially complete within 5 min.

The solids circulation patterns were investigated with a force probe developed in-house. Typical force probe responses are presented in Figures 10 and 11 for a probe located at 0.13 m from the jet nozzle and with different penetrations into the bed for an

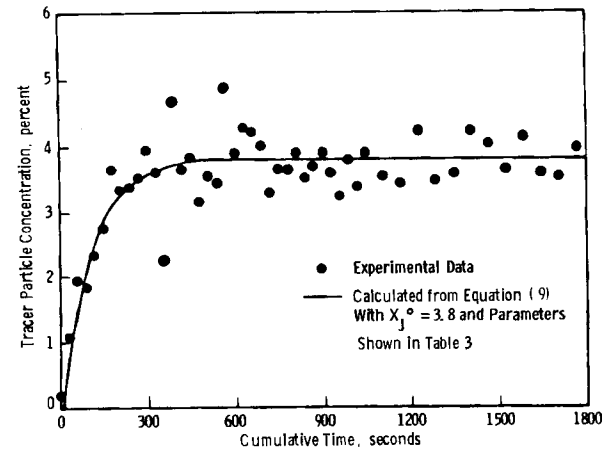

Figure 7. Experimental solids mixing data and model predictions.
0.254 m jet; set point 3; sampling port C.

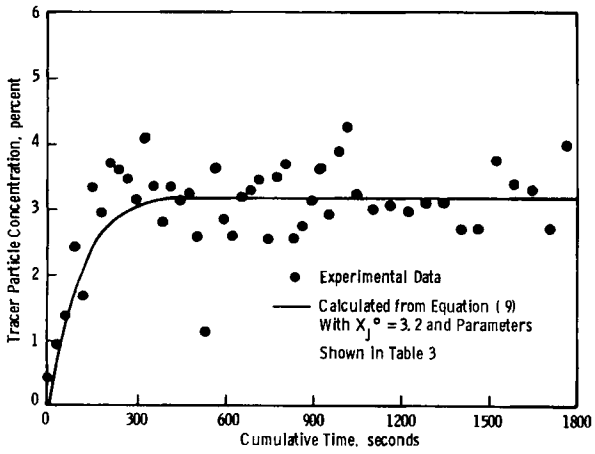

Figure 8. Experimental solids mixing data and model predictions.
0.254 m jet; set point 3; sampling port D.

air tube velocity of 45.7 m/s. Since the force probe is directional, the upward solids movement will produce a positive response from the probe and vice versa, the magnitude of the response being an indication of the magnitude of solids circulation rate. The number of major peaks per unit time is closely related to the actual bubble frequency in the bed.

Solids Circulation Patterns

The force probe data allow the identification of three major solids flow regions in the 3 m model, as shown in Figure 12. At the central portion of the bed, the solids flow is induced upward primarily by jetting action at the lower bed height and by large bubbles at the higher bed height. At the outer region next to the vessel wall, the solids flow is all downward. The region has a thickness of approximately 0.25 m. Between these two regions the solids flow is alternatively upward and downward, depending on the approach and departure of large bubbles. No stagnant region was evident anywhere in the bed. Figure 12 was constructed on the basis of the force probe signal. At the central portion of the bed where the solids flow was upward, the probe gave a positive signal while the signal in the outer region was all

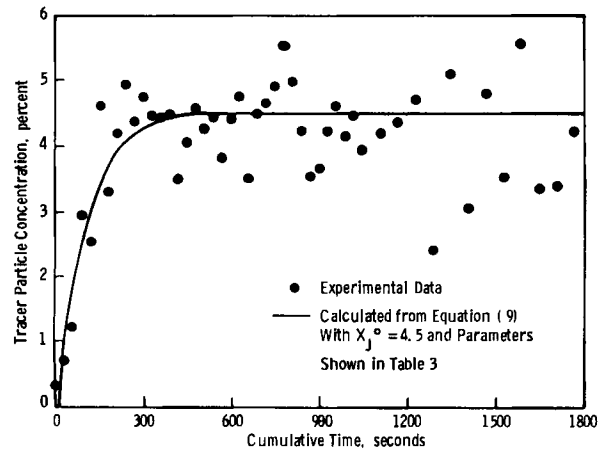

Figure 9. Experimental solids mixing data and model predictions.
0.254 m jet; set point 3; sampling port E.

Table 2. Bed Operating Conditions, 0.406 m Jet Nozzle Assembly

	Set Point No.	
	1	2
Air tube flow, m^3/min*	47.5	100.3
Annular flow, m^3/min	8.1	8.4
Total grid flow, m^3/min	94.5	94.3
Solids transport flow, m^3/min	24.9	25.8
Total tracer injected, kg	255	241
Tracer injection time, s	165	75
Freeboard velocity, m/s	0.71	0.90

*Flow rates expressed at standard conditions of 20°C and 101 kPa.

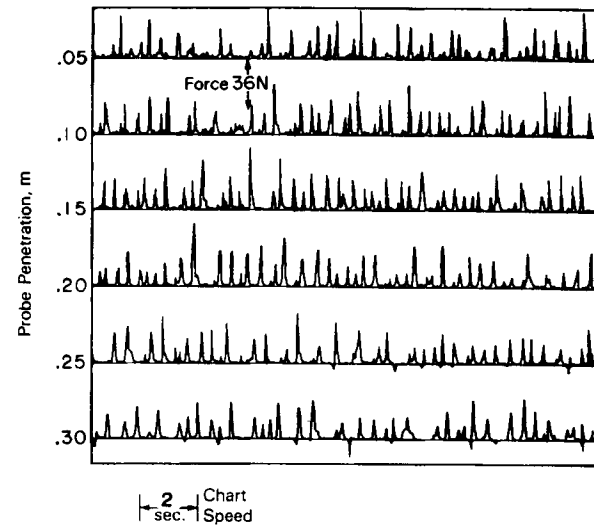

Figure 10. Force probe responses 0.13 m from jet nozzle; 46 m/s air tube velocity, no solid feed.

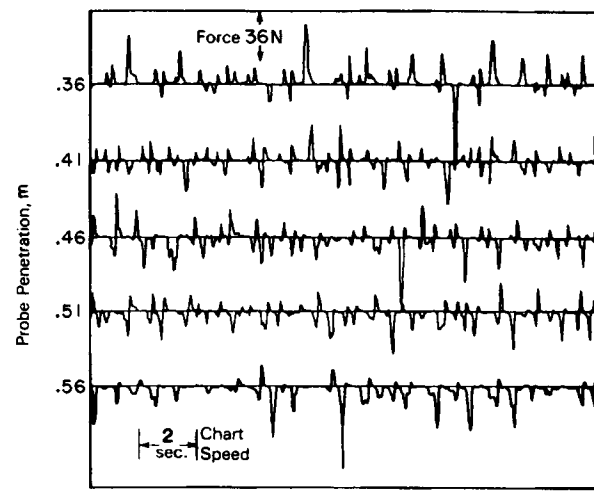

Figure 11. Force probe responses 0.13 m from jet nozzle; 46 m/s air tube velocity, no solid feed.

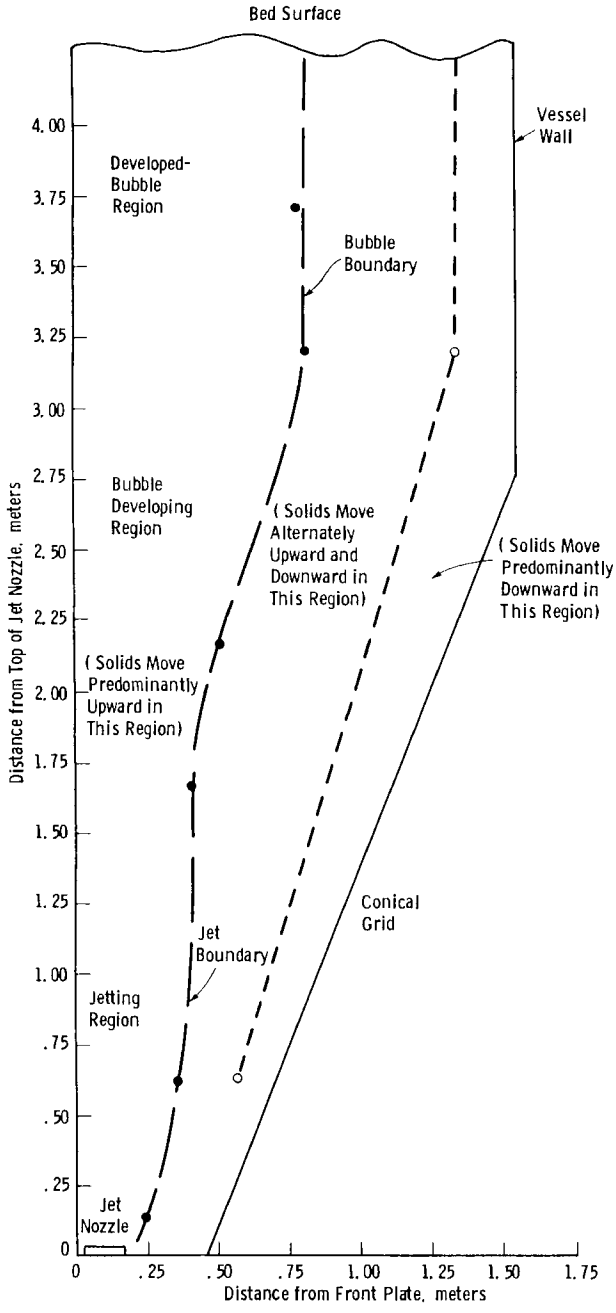

Figure 12. Three major solids flow regions in 3 m model derived from force probe signal.

negative because the solids flow was predominantly downward. The radial position where the first negative signal was observed was taken as the boundary between the central region and the intermediate region. The probe penetration where the probe signal became all negative was taken as the transition between the intermediate region and the outer region.

In addition to the three solids circulation regions readily identifiable, the approximate jet penetration depth and bubble size can also be obtained from Figure 12. The jetting region can be taken to be the maximum average value of jet penetration depth. From the jet boundary at the end of the jetting region, an initial bubble diameter can be estimated. This value can be taken to be the minimum value of the initial bubble diameter. The diameter of a fully developed bubble can be obtained from the bubble boundary in the developed-bubble region, as shown in Figure 12. The central region is thus divided further into three separate regions axially: the jetting region, the bubble-developing region, and the developed-bubble region. Bubbles were observed to coalesce in the bubble-developing region during analysis of the motion pictures taken through the transparent front plate.

Development of a Mathematical Model for Solids Mixing

A simple mechanistic model was developed to correlate the data. The model assumes that the solids circulation inside the bed is induced primarily by the bubble motion. The solids circulation pattern inside the bed can be divided into two major regions radially. In the center of the bed, the particle movement is predominantly upward and the movement is induced by the bubbles disengaged from the central jet. We call this region the "bubble street" because it is the path of all bubbles generated from the jet. This region has a radius similar to the radius of the average bubble size. In the outer region, the particles move primarily downward. In the meantime, the particles in both regions exchange with each other across the neighboring boundary at a constant rate of W_z g/cm^2 · s. This mechanistic model is shown schematically in Figure 13. Material balance in a differential element dz as shown in Figure 13 gives:

In the bubble street region

$$K\frac{\partial X'_J}{\partial Z} + \pi R_i^2(1-\epsilon_{mf})\rho_s\frac{\partial X'_J}{\partial t} + 2\pi R_i W_z(X'_J - X_J) = 0 \quad (1)$$

In the annular region

$$K\frac{\partial X_J}{\partial Z} + \pi(R_o^2 - R_i^2)(1-\epsilon_{mf})\rho_s\frac{\partial X_J}{\partial t} + 2\pi R_i W_z(X_J - X'_J) = 0 \quad (2)$$

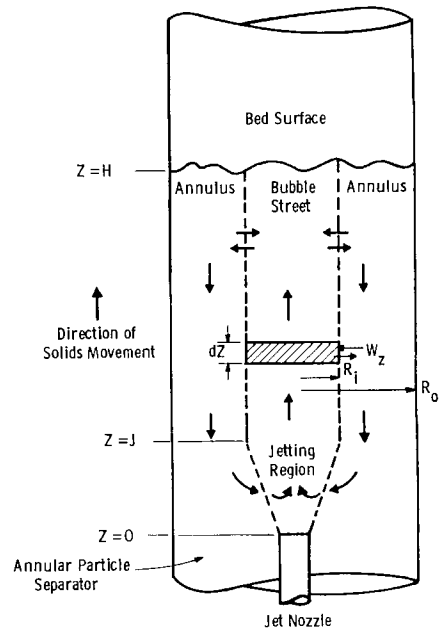

Figure 13. Mechanistic model for solids mixing.

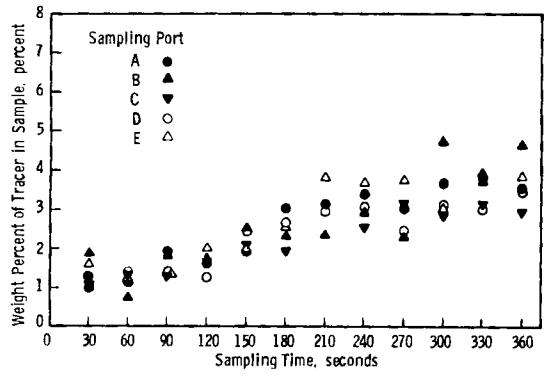

Figure 14. Cross plot of experimental data, 0.406 m jet, set point 1, showing no clear axial dependence.

where

$$K = nV_B f_w (1 - \epsilon_w)\rho_s \tag{3}$$

Equations 1 and 2 are coupled, and analytical solutions cannot be easily obtained even with boundary conditions clearly identified. Because of the scatter in the data, numerical solution does not have any added advantages because the axial variations of the concentration profiles will have to be obtained from the experimental data. This can be clearly shown by cross-plotting the experimental data vs. time for different sampling ports, as shown in Figure 14. The data do not show any clear dependence on the axial position, z. For the subsequent development, the axial dependence is thus assumed to be negligible. With the limited experimental data available so far, a first approximation of negligible axial dependence is reasonable. Equations 1 and 2 are reduced from partial differential equations to ordinary differential equations. If we consider only the annular region, Eq. 2 reduces to

$$\frac{dX_J}{dt} + \frac{2\pi R_i W_z}{\pi(R_o^2 - R_i^2)(1 - \epsilon_{mf})\rho_s}(X_J - X'_J) = 0 \tag{4}$$

Since both X_J and X'_J are independent of z, the relationship betwen X_J and X'_J can be approximated by material balance of the coarse particles injected into the bed to serve as the tracer.

Solving for X'_J, we have

$$X'_J = \frac{W_t}{\pi R_i^2 H(1 - \epsilon_{mf})\rho_s} - \left[\left(\frac{R_o}{R_i}\right)^2 - 1\right]\left(\frac{1 - \epsilon_{mf}}{1 - \epsilon_i}\right)X_J \tag{5}$$

Substituting Eq. 5 into Eq. 4, and after some mathematical manipulation, we get

$$\frac{dX_J}{dt} + PX_J - Q = 0 \tag{6}$$

where

$$P = \frac{2R_i W_z}{(R_o^2 - R_i^2)(1 - \epsilon_{mf})\rho_s} + \frac{2W_z}{R_i(1 - \epsilon_i)\rho_s} \tag{7}$$

$$Q = \frac{2W_z W_t}{\pi R_i(R_o^2 - R_i^2)H(1 - \epsilon_{mf})(1 - \epsilon_i)\rho_s^2} \tag{8}$$

Equation 6 can be readily integrated, however, there are two limiting cases to consider.

Case I. Instantaneous Injection of Tracer Particles. If it is assumed that the tracer particles are injected instantaneously, $W_t = W_t^o$ = a constant, Eq. 6 can be integrated with the boundary condition that $X_J = 0$ at $t = t_o$ to give

$$\frac{X_J}{X_J^o} = 1 - \exp\left[-P(t - t_o)\right] \tag{9}$$

Case II. Uniform Injection of Tracer Particles. Since the large amount of tracer particles usually required more than 75 s to inject, the other limiting case would be to assume that the injection rate was uniform over the injection period, or

$$W_t = \left(\frac{W_t^o}{t_w}\right)t \tag{10}$$

Again, Eq. 6 can be integrated with the boundary condition that $X_J = 0$ at $t = 0$ to give

$$\frac{X_J}{X_J^o} = \frac{1}{t_w P}\{Pt - [1 - \exp(-Pt)]\} \tag{11}$$

Equation 11 is applicable only between $t = 0$ and $t = t_w$. For $t > t_w$, Eq. 9 can be applied by setting $t = t - t_w$ and $X_J = X_J - (X_J)_{t_w}$, where $(X_J)_{t_w}$ is the tracer concentration at time t_w.

The equilibrium tracer concentration in the bed after complete mixing can be expressed as

$$X_J^o = \frac{W_t}{\pi H \rho_s[R_i^2(1 - \epsilon_i) + (R_o^2 - R_i^2)(1 - \epsilon_{mf})]} \tag{12}$$

The voidage inside the bubble street, ϵ_i, can be calculated as follows

$$\epsilon_i = \epsilon_{mf} + f_B(1 - \epsilon_{mf}) = \epsilon_{mf} + \frac{nV_B}{\pi R_i^2 U_A}(1 - \epsilon_{mf}) \tag{13}$$

where f_B is the volumetric fraction of bubbles occupying the bubble street region at any instant; it can be evaluated from the following equation:

$$f_B = \frac{nV_B}{\pi R_i^2 U_A} \tag{14}$$

If the bubble frequency, bubble diameter, and bubble velocity are known, the solids mixing rate can be calculated.

Solids Mixing Rates in Various Bed Configurations

The mechanistic model developed in the last section is applied to the data collected experimentally. Bubble diameter and bubble velocity calculations were based on the empirical equations obtained from frame-by-frame analysis of high-speed motion pictures taken under the respective operating conditions (Yang

et al., 1984). The equations used are:

For 0.254 m jet nozzle assembly

$$\text{Bubble diameter} \quad D_B = 12.36\, G^{0.155} \tag{15}$$

$$\text{Bubble velocity} \quad U_A = 0.711\sqrt{gD_B} \tag{16}$$

For 0.406 m jet nozzle assembly

$$\text{Bubble diameter} \quad D_B = 0.0195\, G^{0.620} \tag{17}$$

$$\text{Bubble velocity} \quad U_A = 0.35\sqrt{gD} \tag{18}$$

In correlating the data, the solid exchange rate between the two regions, W_z, was assumed to be constant. The model was applied only to the bed height beyond the bubble coalescing region (or jetting region). The bubbles were already completely coalesced during their transit through the bubble street. The bubble frequency was then assumed to be constant at a rate of 30 cycles per min experimentally found during earlier studies employing motion pictures and force probe (Yang et al., 1984). Because of scattering in the data, neither Eq. 9 at $t_o = 0$ nor Eq. 11 is optimum in extracting the radial mixing flux, W_z. The tracer concentration data were analyzed statistically and the best fit was found to be provided by Eq. 9 with statistically fitted t_o, as shown in Table 3.

It can be seen that the intersections at the abscissa, the time zero t_o, are always close to zero or positive. That means the coarse tracer particles did not appear in the solids samples in the early part of the experiment. This is to be expected because it took more than 75 s to inject the tracer particles into the bed. The slopes of the straight lines can be taken to be the net solids exchange fluxes between the bubble street and the annular region; they are reported in Table 3. The positive fluxes indicate that the net solids flow is from bubble street to annular region. The net exchange fluxes do not seem to depend on the jet velocity and the bed configuration, as shown in Table 3. The solids circulation rate depends on the jet velocity, however, because higher jet velocities generate larger bubbles. The circumferential area surrounding the bubble street will then be larger and thus the solids circulation rate will be larger. The solids circulation rates derived on the basis of this model range from 47,500 to 73,400 kg/h, as shown in Table 3.

Comparison of the calculated and the experimentally observed tracer concentration profiles is good as shown in Figures 5 through 9 for set point 3 employing the 0.254 m jet nozzle assembly. Similar comparisons were obtained for other experimental data as well.

Conclusions

The force probe data allow the identification of three major solids flow regions in a large jetting fluidized bed. At the central portion of the bed the solids flow is induced upward primarily by jetting action at the lower bed height and by large bubbles at the higher bed height. At the outer region next to the vessel wall, the solids flow is predominantly downward. In between these two regions the solids flow is alternatively upward and downward, depending on the approach and departure of large bubbles.

The solids mixing study by injection of tracer particles indicated that the axial mixing of solids in the bubble street is apparently very fast. Radial mixing flux depends primarily on the bubble size, bubble velocity, and bubble frequency, which in turn depend on the size of the jet nozzle employed and the operating jet velocity. A simple mechanistic model was developed that divided the bed into two separate regions, the bubble street where the solids move predominantly upward, induced by the bubbles, and the annular region where the particles move primarily downward. There is a net solids flow radially from the bubble street to the annular region. The solids then flow downward in the annular region and eventually are reentrained into the jetting region, as shown in Figure 13. Besides the statistical analysis of the experimental data to extract the parameter t_o, the model makes no other assumptions. The experimental bubble size, bubble velocity, bubble frequency, and jet penetration depth extracted from frame-by-frame analysis of high-speed motion pictures were used in correlating the solids mixing data. It is believed that the model adequately describes the solids circulation pattern and the solids mixing rate in a large jetting fluidized bed.

Table 3. Statistical Analysis of Solids Mixing Data

Test No.	t_o s	W_Z kg/m^2 s	$2\,R_i W_Z(H-J)$ kg/s
0.254 m Jet Nozzle Assembly			
Set Pt. 1	8.3	1.0	13.2
Set Pt. 2	44.5	1.3	16.2
Set Pt. 3	10.2	1.3	17.7
Set Pt. 4	−10.2	1.0	13.4
0.406 m Jet Nozzle Assembly			
Set Pt. 1	−1.2	1.0	14.7
Set Pt. 2	−8.6	0.84	20.4

Acknowledgment

This work is carried out under U.S. Department of Energy Contract No. DE-AC21-82MC19122. The experiments described in this paper were performed by M. T. Barbor, E. E. Catalina, R. A. Crowe, J. H. Crum, R. E. Gizzie, C. J. Lang, R. D. Novak, and J. E. Pietraszewski.

Notation

D = diameter of a fluidized bed
D_B = gas bubble diameter
f_B = volumetric fraction of bubble in bubble street
f_w = wake fraction of the bubble
g = gravitational acceleration
G = total volumetric flow rate through jet nozzle assembly
H = bed height of fluidized bed
J = jet penetration depth
n = bubble frequency
R_i = radius of bubble street, $R_i = D_B/2$
R_o = bed radius
t = time
t_o = time zero, Eq. 9
t_w = total time required to inject all trace particles
U_A = absolute bubble velocity
V_B = bubble volume
W_i^o = total weight of tracer particles injected
W_t = cumulative weight of tracer particles injected after time t
W_z = radial solids mixing flux
X_J^o = tracer particle weight fraction in the bed after complete mixing
X_J, X_J' = tracer particle weight fractions in annulus and in bubble street respectively
z = axial coordinate
ϵ_i = voidage in bubble street

ϵ_{mf} = voidage at minimum fluidization
ϵ_w = voidage in bubble wake
ρ_s = solid particle density

Literature cited

Kunii, D., and O. Levenspiel, *Fluidization Engineering,* Wiley, New York, 140 (1969).

Potter, O. E., "Mixing," *Fluidization,* J. F. Davidson and D. Harrison, eds., Academic Press, London, 233 (1971).

Valenzuela, J. A., and L. R. Glicksman, "An Experimental Study of Solids Mixing in a Freely Bubbling Two-Dimensional Fluidized Bed," *Powder Tech.,* **38,** 63 (1984).

Yang, W. C., E. Ettehadieh, T. C. Anestis, R. E. Gizzie, and G. B. Haldipur, "Cold Flow Scale-up Facility Experimental Results and Comparison of Performance at Different Bed Configurations," KRW Energy Systems Inc. for U.S. Dept. Energy, Contract No. DE-AC21-82MC19122; NTIS No. FE-19122-46 (July, 1984).

Manuscript received July 25, 1985, and revision received April 14, 1986.